Interactive Monte Carlo Denoising using Affinity of Neural Features

MUSTAFA IŞIK, Technical University of Munich, Germany
KRISHNA MULLIA, Adobe, California, USA
MATTHEW FISHER, Adobe, California, USA
JONATHAN EISENMANN, Adobe, California, USA
MICHAËL GHARBI, Adobe, California, USA

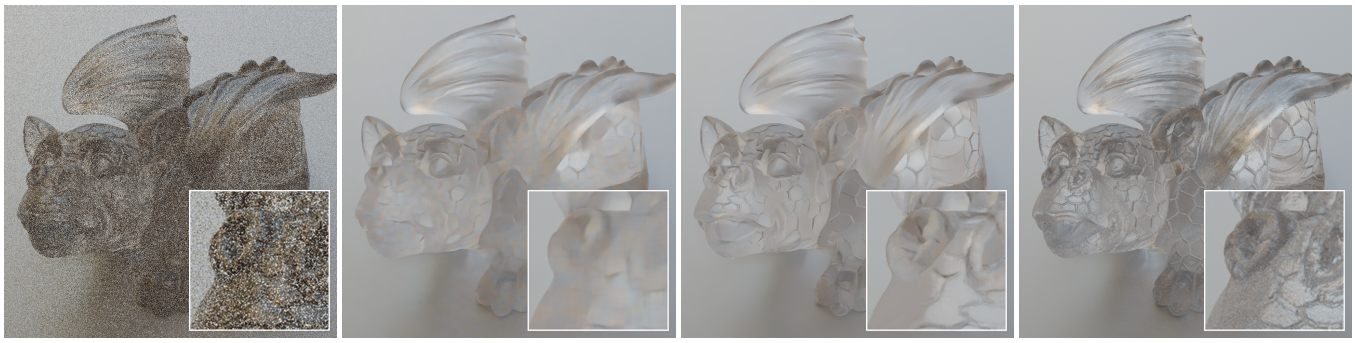

(a) input (8 spp) (b) Munkberg and Hasselgren [2020] PSNR = 26.6 dB, **435ms** (c) ours PSNR = 27.2 dB, **97 ms** (d) reference (4096 spp)

Fig. 1. Our denoiser targets images from interactive path-tracers with low sample per pixel (spp) budget (a). It runs at interactive rates and produces temporally-stable, high-quality results (c), with better details and fewer artifacts than state-of-the-art off-line denoisers (b), and significantly outperforms interactive denoisers (not shown). Timings are recorded using PyTorch implementations on a GeForce RTX 2080 Ti graphics card. See Table 1 for our optimized implementation that runs interactively. The reference (d) was rendered with a much higher computational budget. The resolution is 1024×1024.

High-quality denoising of Monte Carlo low-sample renderings remains a critical challenge for practical interactive ray tracing. We present a new learning-based denoiser that achieves state-of-the-art quality and runs at interactive rates. Our model processes individual path-traced *samples* with a lightweight neural network to extract per-pixel feature vectors. The rest of our pipeline operates in pixel space. We define a novel pairwise affinity over the features in a pixel neighborhood, from which we assemble dilated spatial kernels to filter the noisy radiance. Our denoiser is temporally stable thanks to two mechanisms. First, we keep a running average of the noisy radiance and intermediate features, using a per-pixel recursive filter with learned weights. Second, we use a small temporal kernel based on the pairwise affinity between features of consecutive frames. Our experiments show our new affinities lead to higher quality outputs than techniques with comparable computational costs, and better high-frequency details than kernel-predicting approaches. Our model matches or outperfoms state-of-the-art offline denoisers in the low-sample count regime (2–8 samples per pixel), and runs at interactive frame rates at 1080p resolution.

CCS Concepts: • **Computing methodologies** → **Ray tracing**; **Neural networks**.

Additional Key Words and Phrases: Monte Carlo denoising, deep learning

Authors' addresses: Mustafa Işık, Technical University of Munich, Munich, Germany, m.isik@tum.de; Krishna Mullia, Adobe, San Jose, California, USA, mulliala@adobe.com; Matthew Fisher, Adobe, San Francisco, California, USA, matfishe@adobe.com; Jonathan Eisenmann, Adobe, San Francisco, California, USA, j@adobe.com; Michaël Gharbi, Adobe, San Francisco, California, USA, mgharbi@adobe.com.

ACM Reference Format:
Mustafa Işık, Krishna Mullia, Matthew Fisher, Jonathan Eisenmann, and Michaël Gharbi. 2021. Interactive Monte Carlo Denoising using Affinity of Neural Features. *ACM Trans. Graph.* 40, 4, Article 37 (August 2021), 13 pages. https://doi.org/10.1145/3450626.3459793

1 INTRODUCTION

Rendering noise-free path-traced images at interactive frame rates remains an elusive objective despite the advent of hardware raytracing accelerators and GPU raytracing APIs [Khronos 2020; Microsoft 2021; Parker et al. 2013]. The fastest modern GPUs can only afford to trace a handful of samples per pixel in real time for typical display resolutions, leading to severe noise in the renderings.

State-of-the-art Monte Carlo denoisers use large kernel-predicting neural networks [Bako et al. 2017; Gharbi et al. 2019; Kettunen et al. 2019; Vogels et al. 2018; Xu et al. 2019]. Their computational cost is rarely an issue for off-line rendering, since raytracing dominates the overall latency, but it is impractical for interactive applications. The fastest denoisers typically use hand-designed filters [Mara et al. 2017] or much more compact neural networks [Chaitanya et al. 2017; Meng et al. 2020] that sacrifice quality for performance. Denoising artifacts are often amplified in video animation where care must be taken to create temporally stable results that do not contain high-frequency artifacts between adjacent frames. The shortcomings of interactive denoisers are particularly salient around soft shadows, complex global illumination, glossy reflections and refractive materials — precisely where raytracing has the most appeal.

We present a new denoiser for low-sample, interactive raytracing applications that directly operates on the path-traced samples. Our model is a lightweight neural network (~940k parameters) that summarizes rich per-sample information into low-dimensional per-pixel feature vectors. We define a novel pairwise affinity over these features, which we use to weight the contributions of neighboring per-pixel radiance values in a local weighted average filtering step. These new affinity-based kernels lead to better denoising performance compared to kernel-predicting techniques [Bako et al. 2017; Gharbi et al. 2019; Munkberg and Hasselgren 2020; Vogels et al. 2018], especially when reconstructing fine details, or in high-frequency light transport configurations.

We evaluate our denoiser on a diverse set of static renderings and fly-through animations. We show it produces much cleaner outputs and lower numerical error than state-of-the-art interactive denoisers with comparable runtime cost. For low-sample count renderings, our model even matches or outperforms the state-of-the-art off-line denoisers, for a fraction of the computational cost (Figure 1). In short, our contributions are the following:

- A state-of-the-art denoiser for low-sample count Monte Carlo rendering that runs at interactive rates and outperforms the quality of even powerful off-line baselines in the low-sample count regime,
- A novel filtering algorithm that uses pairwise affinity of per-pixel deep features learned from the raw path-tracing samples to learn iteratively-applied 2D dilated kernels,
- A new temporal aggregation mechanism which uses the same pairwise affinity to significantly improve the temporal stability of Monte Carlo denoising.

2 RELATED WORK

With the advent of powerful hardware accelerators, ray-tracing has become viable for real-time rendering. But, because today's GPUs can only trace a few samples at interactive rates, fast high-quality denoisers remain critical. We discuss the most recent related work, and refer the reader to Zwicker et al. [2015] for an overview of denoising techniques.

Traditional adaptive sampling and reconstruction. A priori methods approach denoising as a reconstruction problem, deriving filters and sampling strategies from an analysis of light transport [Belcour et al. 2013; Durand et al. 2005; Egan et al. 2011, 2009; Lehtinen et al. 2012]. *A posteriori* methods inspired our affinities, which strictly generalize the bilateral filter. Prior works have explored multi-dimensional path space analysis [Hachisuka et al. 2008], multiscale filters [Overbeck et al. 2009; Rousselle et al. 2011], image-denoising filters [Kalantari and Sen 2013; Rousselle et al. 2012], cross-bilateral filters [Li et al. 2012; Rousselle et al. 2013], and local regressions [Bitterli et al. 2016; Moon et al. 2014, 2016], often jointly addressing adaptive sampling.

Machine-Learning based image-space methods. Recent work has used neural networks for denoising, avoiding the need to manually tune filter parameters for each scene. Kalantari et al. [2015] use a fully-connected neural network and predict the parameters of a cross-bilateral filter. Bako et al. [2017] showed that a convolutional network that predicts per-pixel filtering kernels is more robust and easier to train than models that directly output the denoised radiance. Vogels et al. [2018] extended this technique with multiscale filtering [Delbracio et al. 2014], temporal aggregation and adaptive sampling. Xu et al. [2019] use a generative adversarial training procedure to improve image quality. Kuznetsov et al. [2018] predict sampling density maps for adaptive sampling. Our denoiser also uses kernels, but instead of predicting the full-rank kernels, our network outputs feature vectors for each pixel from which we define pairwise affinities. This makes the learning problem simpler, which leads to a more parsimonious model, suitable for interactive use.

Sample-based image-space methods. These methods strive to fully exploit per-sample information to maximize denoising quality. Sen and Darabi [2012] use per-sample cross-bilateral filters to filter the noise caused by random parameters in the Monte Carlo integration. Gharbi et al. [2019] use a neural network for sample-based denoising. They predict splatting kernels for each sample, and take special care in ensuring their network is invariant to permutation of the samples within a pixel. Their method scales poorly for interactive rendering settings because the network evaluation cost grows linearly with the number of samples. Munkberg and Hasselgren [2020] mitigate this issue by partitioning and averaging the samples into a fixed number of layers, filtering the layers independently, and compositing them front to back. Our method also processes individual samples but applies kernels to *per-pixel* averages not samples, which significantly reduces the runtime cost.

Interactive denoising. Denoisers designed for interactive applications focus on efficiency and temporal stability. Early techniques used hierarchical wavelet filters and edge-stopping functions based on auxiliary render buffers [Dammertz et al. 2010] or edge-aware guided filters [Bauszat et al. 2015, 2011; He et al. 2010]. Schied et al. [2017] used a fixed-weight recursive temporal smoothing filter for temporal stability, which Schied et al. [2018] improved by using adaptive temporal accumulation weights. We also use adaptive temporal accumulation in our temporal smoothing strategy, with weights predicted by our network, but complement it with a temporal kernel computed with our new affinity. Koskela et al. [2019] brings regression-based denoising to the real-time domain. Chaitanya et al. [2017] achieve high-quality, temporally-stable results at interactive frame rates using a recurrent U-net [Ronneberger et al. 2015]. Hasselgren et al. [2020] extend the work of Kuznetsov et al. [2018] to the temporal domain and obtain better temporal stability than Chaitanya et al. [2017] by using motion vectors to warp the previous prediction. Meng et al. [2020] splat the noisy radiance into a bilateral grid. Slicing in the grid along a learned guidance map gives the denoised output. They also use a recursive filter with fixed weight for temporal stability. We discuss the similarities between the neural bilateral grid and our affinities in Section 3.7. Our adaptive temporal accumulation improves denoising performance, in particular around occlusions and specular reflections. Our affinity-based temporal kernel further improves temporal stability, removing low-frequency noise and enlarging the filter's footprint in time.

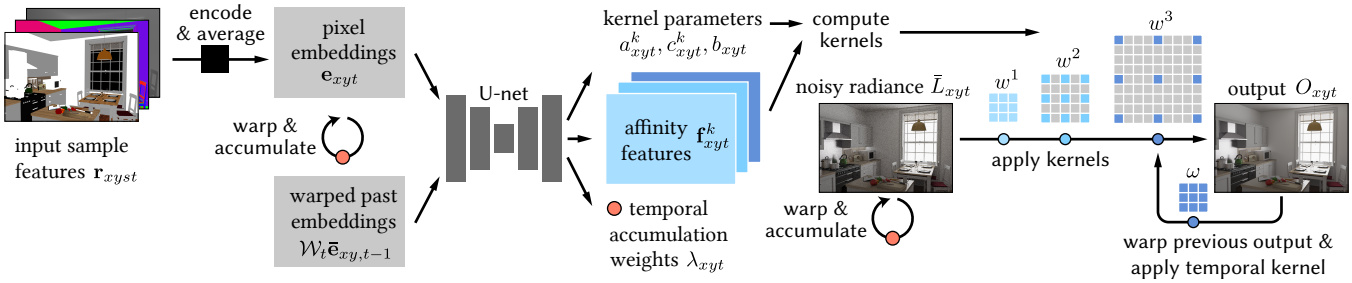

Fig. 2. **Pipeline overview.** We encode the individual samples with a fully connected network, then average them to obtain per-pixel neural embeddings. We concatenate these embeddings with the warped embeddings from the previous frame and process them with a U-Net to generate kernel parameters, affinity features, and a temporal accumulation weight for each pixel. We compute dilated 2D kernels from the affinity and apply them iteratively to the noisy input radiance, which is also temporally accumulated. Finally, we use a temporal kernel to blend in the previous denoised output, to get the final, denoised image.

3 DENOISING WITH LEARNED PAIRWISE AFFINITY

The key novelty in our approach is a pairwise affinity measure on learned neural features, from which we derive spatio-temporal filtering kernels to denoise the frames of an animation. We work with samples from a pathtracer [Kajiya 1986] with render buffer features $\mathbf{r}_{xyst}$ (§ 3.1), where (x, y) are the pixel coordinates, $s \in \{1, \ldots, S\}$ are the sample indices within a pixel, and $t \in \{1, \ldots, T\}$ are the frame indices. In interactive applications the number of samples per pixel is typically low ($S < 8$), making temporal stability challenging. Our model addresses this via two mechanisms: first, we use recursive filters with adaptive, per-pixel parameters to maintain running averages of neural embeddings and noisy radiance; second, we apply our denoising kernels to *pairs* of frames.

We visualize our method in Figure 2. We start by independently extracting *per-sample* embeddings $\mathbf{e}_{xyt}$ from each sample's render buffer data using a small pointwise network (§ 3.2). This is the only operation on the raw samples. We use a temporal recursive filter over the embeddings with adaptive learned parameters to propagate information between frames and then average the sample embeddings over all samples in each pixel. From these per-pixel embeddings, we predict a vector of parameters for each pixel using a convolutional network (§ 3.3); convolutions enable information-sharing between neighboring pixels. We use the per-pixel parameters to construct filtering kernels at each pixel (§ 3.4), which we apply to the noisy radiance to obtain the final, denoised output (§ 3.5.2). We decompose the kernels into a sequence of $K = 3$ dilated 2D kernels [Dammertz et al. 2010; Holschneider et al. 1990; Yu and Koltun 2016] with increasing dilation, applied sequentially (§ 3.5.1), followed by a temporal kernel (§ 3.5.2). Dilation enables larger spatial footprints, which helps remove low-frequency noise, but has a minimal impact on performance relative to using large dense kernels. The temporal kernel is built from the affinity between features of the current and previous frames; it smoothes the output over time.

3.1 Input path-traced sample features

Previous work showed that working with samples rather than pixel averages can improve denoising [Gharbi et al. 2019; Hachisuka et al. 2008; Lehtinen et al. 2011, 2012], but can incur a significant computational overhead (see Section 5.4). Similarly to [Munkberg and Hasselgren 2020], we adopt a hybrid strategy: we use per-sample information to compute filtering weights, but the filters operate on the integrated (box-filtered) pixel radiance $\mathbf{L}_{xyt}$, not the samples.

During rendering we store, for each sample, a vector of 18 render buffer features $\mathbf{r}_{xyst}$, which we describe next. First, we store the radiance, split into *diffuse* and *specular* components [Bako et al. 2017], both tonemapped with $x \mapsto \log(1 + x)$ to compress their dynamic range. This tonemapping is only used for the sample input features passed to the network; our denoising kernels operate on the *linear* radiance. We treat materials with roughness below a fixed threshold (0.1 linear roughness in PBRT-v3) as specular. Second, we use the *normal* (3), and *depth* (1) as geometric features. And third, we characterize materials by their *roughness* (1), *albedo* (3), and 4 binary variables: *emissive* — indicates whether the path sampled hits emissive surface, *metallic* — differentiates between dielectric and conductors, *transmissive* — distinguishes between reflections and refractions, and *specular-bounce* — which is 'true' if first vertex on the camera path is a specular interaction. Except the radiance, all features are computed at the first non-specular interaction.

3.2 Mapping samples to per-pixel features

Given our interactivity constraints, we keep per-sample processing to a minimum. We independently embed the samples using a shallow fully-connected network, then reduce the embeddings to per-pixel summary statistics by averaging over the sample dimension:

$$\mathbf{e}_{xyt} = \frac{1}{S} \sum_{s=1}^{S} \mathrm{FC}(\mathbf{r}_{xyst}). \tag{1}$$

This fully-connected network uses leaky ReLU activations. It has 3 layers with 32 channels each. In Section 5.5.2, we show this embedding strategy outperforms the simple first and second-order statistics of raw render buffers used in previous work [Bako et al. 2017; Vogels et al. 2018] for low-spp renderings (2–8 spp).

3.3 Spatio-temporal feature propagation

We next process the per-pixel embeddings with a lightweight U-net [Ronneberger et al. 2015]. This network takes as input the embeddings of both the current and previous frames and produces, for each pixel, a set of feature vectors $\mathbf{f}^k_{xyt} \in \mathbb{R}^d$, and scalars a^k_{xyt} and c^k_{xyt}, for $k = 1, \ldots, K$. We use these parameters and features to compute K dilated spatial kernels, which we apply sequentially to

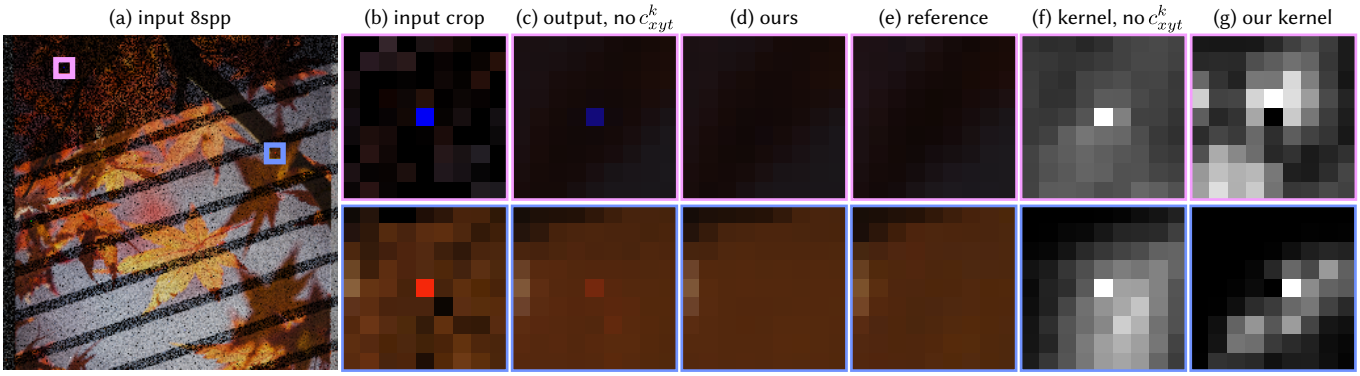

Fig. 3. **Outlier rejection using c^k_{xyt}.** Using an independent variable for the central weight of our kernel in Equation (4) helps suppressing outliers. In this example, we added a random perturbation on the input (a) samples, with a value up to 500× the mean of the image (b). Our ablation without the center weight c^k_{xyt} cannot suppress these outliers (c) because the central weight of its kernels is always $w^k_{xyxyt} = 1$ (f). Our method can easily turn off the outlier (d) by modulating the kernel's central weight (g).

denoise the frame (§ 3.4). Specifically, we compute the spatial kernels by calculating distances between affinity features $\mathbf{f}^k_{xyt}$, scaled by the bandwidth parameters a^k_{xyt}, and c^k_{xyt} is the kernel's central weight. The network also outputs two additional scalars for our temporal filtering mechanisms: b_{xyt} is a bandwidth parameter modulating the feature affinity between successive frames in a temporal kernel; and λ_{xyt} is the parameter of an exponential moving average filter that accumulates the pixel embeddings and noisy radiance temporally (Eq. (3) and (5)). Our implementation uses $K = 3$. Formally, the U-net's output is given by:

$$\left(\mathbf{f}^k_{xyt}, a^k_{xyt}, c^k_{xyt}\right), b_{xyt}, \lambda_{xyt} = \text{UNet}\left(\mathbf{e}_{xyt}, \mathcal{W}_t \bar{\mathbf{e}}_{xy,t-1}\right). \quad (2)$$

$\mathcal{W}_t \cdot$ is a warping operator that reprojects frame $t-1$ to frame t with nearest neighbor interpolation using the geometric flow at the primary intersection point computed by the path tracer [Schied et al. 2017]. And, $\bar{\mathbf{e}}_{xy,t-1}$ is a temporal accumulation of the pixel embeddings defined by:

$$\begin{cases} \bar{\mathbf{e}}_{xy0} &= \mathbf{e}_{xy0}, \\ \bar{\mathbf{e}}_{xyt} &= (1-\lambda_{xyt})\mathbf{e}_{xyt} + \lambda_{xyt}\mathcal{W}_t\bar{\mathbf{e}}_{xy,t-1}. \end{cases} \quad (3)$$

This temporal accumulation of the embeddings helps make temporally consistent predictions, compared to simply passing the previous frame's embeddings (i.e., replacing $\bar{\mathbf{e}}_{xy,t-1}$ with $\mathbf{e}_{xy,t-1}$ in Equation (2)). Figure 5 shows the per-pixel blending weights can selectively mask out ($\lambda_{xyt} = 0$) the warped embedding when they are inaccurate due, e.g., to occlusions/disocclusions, or moving reflections not captured in the geometric velocity vectors. We use a sigmoid activation to ensure $\lambda_{xyt} \in [0, 1]$. We discuss alternative temporal accumulation strategies in Section 5.5.4. Our U-net [Ronneberger et al. 2015] has 5 scales. Its structure is given by:

$$\mathbf{c}64\mathbf{c}64\mathbf{d} \rightarrow \mathbf{c}64\mathbf{c}64\mathbf{d} \rightarrow \mathbf{c}64\mathbf{c}64\mathbf{d} \rightarrow \mathbf{c}80\mathbf{c}80\mathbf{d} \rightarrow$$
$$\mathbf{c}96\mathbf{c}96\mathbf{u} \rightarrow \mathbf{c}80\mathbf{c}80\mathbf{u} \rightarrow \mathbf{c}64\mathbf{c}64\mathbf{u} \rightarrow \mathbf{c}64\mathbf{c}64\mathbf{u} \rightarrow \mathbf{c}32\mathbf{c}32,$$

where $\mathbf{c}k$ is a convolution with k channels and 3×3 kernels, $\mathbf{d}$ is a 2×2 maxpooling operator, $\mathbf{u}$ is 2×2 bilinear upsampling. Every convolution except the last has a leaky ReLU activation. We use concatenation in the skip connections.

3.4 Spatial kernels from pairwise affinity

We define our spatial filtering kernels as an affinity over the features $\mathbf{f}^k_{xyt}$ produced by the U-net:

$$w^k_{xyuvt} = \begin{cases} c^k_{xyt} & \text{if } x = u \text{ and } y = v, \\ \exp\left(-a^k_{xyt}\|\mathbf{f}^k_{xyt} - \mathbf{f}^k_{uvt}\|_2^2\right) & \text{otherwise.} \end{cases} \quad (4)$$

In the network, we use a sigmoid activation to ensure the center weight c^k_{xyt} is in $[0, 1]$ and a squaring function to ensure $a^k_{xyt} \geq 0$. The latter variable acts as a bandwidth parameter that adaptively tunes a pixel's sensitivity to feature differences with its neighbors. With higher values, small differences quickly make the weight go to zero, reducing the kernel's effective footprint to a single pixel. As $a^k_{xyt} \rightarrow 0$, the filter becomes progressively insensitive to features discrepancy, and turns into a box filter. We visualize a few kernels and their bandwidth parameter in Figure 4.

Our network predicts central weights adaptively for each pixel. Setting $c^k_{xyt} = 1$, the center pixel contributes fully to the output. With this weight set to $c^k_{xyt} = 0$, the network can suppress the bright outliers that often appear in low-sample renderings when high-energy, low-probability paths are sampled. Figure 3 illustrates this property. Wu et al. [2013] propose a similar strategy to adapt the central weight of non-local mean filters per pixel, but use ad-hoc closed-form expressions rather than these parameters. Previous Monte Carlo denoising methods [Kalantari et al. 2015; Meng et al. 2020] usually suppress outliers in a pre- or post-processing step.

3.5 Temporally-stable kernel-based denoising

Prior to filtering, we accumulate the noisy radiance $\mathbf{L}_{xyt}$ over time. This has a denoising effect in areas where the motion vector-based warping provides useful correspondences — and improves overall temporal stability:

$$\begin{cases} \bar{\mathbf{L}}_{xy0} &= \mathbf{L}_{xy0}, \\ \bar{\mathbf{L}}_{xyt} &= (1-\lambda_{xyt})\mathbf{L}_{xyt} + \lambda_{xyt}\mathcal{W}_t\bar{\mathbf{L}}_{xyt}. \end{cases} \quad (5)$$

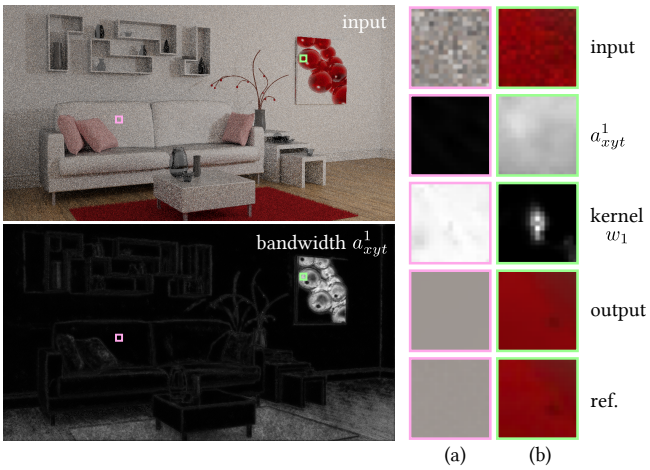

Fig. 4. **Impact of the kernel bandwidth parameter** a^k_{xyt}. Lower bandwidths reduce the kernel sensitivity to feature differences, leading to larger kernels (a). In the limit $a^k_{xyt} \to 0$, we get a box filter. With higher values, the kernels are more selective and peaky (b). The map on the left shows how the bandwidth vary spatially. Our model uses large kernels to smooth out flat areas, but selects smaller kernels where details need to be preserved.

We use the same temporal blending weights λ_{xyt} as for the accumulated embeddings in Equation (3). We use this temporal accumulation as the input for our kernel-filtering step. We obtain the denoised image by sequentially filtering the noisy frame $\bar{\mathbf{L}}_{xyt}$ with $K = 3$ dilated spatial filters, and combining the result with the previous denoised image using a temporal kernel.

3.5.1 Spatial filtering with a sequence of dilated filters. We initialize $\mathbf{L}^{(0)}_{xyt} := \bar{\mathbf{L}}_{xyt}$ and apply the first $K-1$ kernels from Equation (4) sequentially using the following expression:

$$\mathbf{L}^{(k)}_{xyt} = \frac{\sum_{u,v} w^k_{xyuv} \mathbf{L}^{(k-1)}_{uvt}}{\epsilon + \sum_{u,v} w^k_{xyuv}}. \tag{6}$$

The sums run over a square neighborhood with dilation 2^{k-1} (see Figure 2 for an illustration), and $\epsilon = 10^{-10}$ is a small constant to avoid numerical instability. Every time the radiance is filtered, the noise statistics change, so we use different affinities at each step (i.e., different $\mathbf{f}^k_{xyt}$, c^k_{xyt} and a^k_{xyt}). Our implementation uses kernels with 13×13 taps, so the kernel with the largest dilation factor $2^{K-1} = 4$ has an effective footprint of $(13-1) \times 4 + 1 = 49$ pixels in each dimension. Composing the sequential filtering steps gives an overall pixel footprint of 85×85.

3.5.2 Temporal filtering. In our final filtering step, we apply a temporal kernel that measures the affinity between the features of the current and previous frame, after warping, similar to Equation (4):

$$\omega_{xyuvt} = \exp\left(-b_{xyt} \|\mathbf{f}^K_{xyt} - \mathcal{W}_t \mathbf{f}^K_{uv,t-1}\|_2^2\right). \tag{7}$$

Here again, we ensure the bandwidth parameter b_{xyt} is non-negative using a squaring function. This temporal filter uses the same features $\mathbf{f}^k_{xyt}$ as the last spatial kernel (Equation (4) with $k = K$). Note that w^k_{xyuvt} are the spatial kernels and ω_{xyuvt} is the temporal kernel.

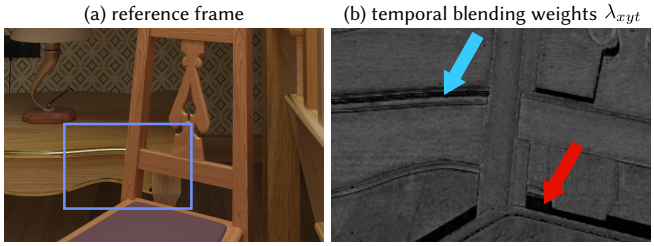

Fig. 5. **Temporal accumulation blending weights.** Our model predicts spatially-varying blending weights $\lambda_{xyt} \in [0,1]$ quantifying how much of the accumulated past radiance and pixel embeddings (not shown) are carried over and blended with the next frame. The weight map (b) shows our model discards parts of the previous frame that were occluded (red arrow), or with large changes in appearance, like specular reflections (blue arrow).

We obtain our final denoised image using this temporal kernel and the last spatial kernel as follows:

$$\mathbf{O}_{xyt} = \frac{\sum_{u,v} w^K_{xyuv} \mathbf{L}^{(K-1)}_{uvt} + \sum_{u',v'} \omega_{xyu'v'} \mathcal{W}_t \mathbf{O}_{u'v',t-1}}{\epsilon + \sum_{u,v} w^K_{xyuv} + \sum_{u',v'} \omega_{xyu'v'}}. \tag{8}$$

The u, v run over a square neighborhood with dilation 2^{K-1}, and u', v' run over a smaller neighborhood, with dilation 1. We also use a 13×13 window for the temporal kernel. Unlike Equation (6), the K-th spatial kernel is jointly normalized with the temporal filter. We use $\omega_{xyuv,0} = 0$ at $t = 0$.

3.6 Comparison to kernel-predicting networks

As shown by Munkberg and Hasselgren [2020]; Vogels et al. [2018], kernel-predicting methods [Bako et al. 2017] require deeper and larger networks to fully benefit from larger kernels. This is because the number and complexity of pairwise interactions between pixels under the kernel increases with kernel size. In contrast, our method does not require such an increase in network "capacity" since we predict per-pixel features with a closed-form affinity, rather than full-rank kernels. In Section 5.5.6, we show our affinity-based kernels are significantly better at reconstructing high-frequency details than gather kernels [Bako et al. 2017].

Additionally, since we compute the kernels *a posteriori* from the learned pixel affinities, we can dynamically change the kernel size at runtime, without retraining. Kernel-predicting networks are limited to the fixed kernel size they were trained with. This property can be used as a dynamic quality–performance trade-off control (§ 5.4). We analyze the effect of kernel size in Section 5.5.3.

3.7 Relation to the neural bilateral grid

Meng et al. [2020] (NBG) use a neural bilateral grid [Gharbi et al. 2017] for denoising, thus approximating a bilateral filter. They use a 3D grid: the first 2 dimensions are the screen-space coordinates, and the third is a learned scalar parameter, which would correspond to the range filter in a traditional bilateral filter [Tomasi and Manduchi 1998]. This is similar to using feature vectors ($\mathbf{f}^k_{xyt}$) with dimension $d = 1$ in our affinities (we use $d = 8$). However, we show this dimension parameter is critical in Section 5.5.1. Setting $d = 1$ leads to oversmoothing (Figure 9) and severely reduces quality (Table 4).

4 DATASET AND TRAINING PROCEDURE

We train our denoiser on randomly generated training scenes (§ 4.1). In total, we collected a training set of 7707 animations in which a camera flies through an otherwise static scene. Each sequence is 8-frame long and rendered at 256×256 resolution. For model selection, we also render a validation with 821 scenes, using the same random generator. Our training objective and procedure are detailed in Section 4.2 and 4.3, respectively.

4.1 Dataset generation

We adapted the scene generator from Gharbi et al. [2019]. Our goal is to cover a wide variety of light transport scenarios, so that our denoiser generalizes to new scenes, by randomizing the scene content and parameters.

Geometry. We use 6 rooms from Tungsten [Bitterli 2016] as background. For each data sample, we choose a room at random and add 50 objects, randomly chosen from ShapeNet [Chang et al. 2015], applying a random rigid transformation to each object. We take the camera position into account for object placement in order to minimize the chance of a completely occluded rendering. The randomness in our generator can still lead to some be completely black renderings which we remove in a post-processing pass.

Lights and materials. Next, each material is randomized by selecting one of the PBRT-v3 materials (e.g., substrate, matte, plastic, disney). To increase the diversity of appearance, we randomly select texture maps from the Describable Textures Dataset [Cimpoi et al. 2014]. We randomly scale each texture for variety in the frequency characteristics. In addition to randomizing the energy of each light source in the background scene, we also insert 2 point light sources with random positions and energies in order to maximize the diversity of the lighting and shadow patterns.

Camera and rendering. Each scene is rendered using a perspective pinhole camera model in PBRT-v3 [Pharr et al. 2016], with a modified path tracer integrator. We randomized the camera's field of view to vary the frequency content of our renderings. As pointed by [Gharbi et al. 2019], PBRT scales ray differentials (to reduce aliasing) based on the sample count. This causes discrepancies in appearance between the low-sample input and ground truth, so we use a constant scaling factor instead. We render the noisy inputs using 8 samples per pixels, storing the samples individually so we can randomize the number of samples at the training time. We render the ground truth at 2048 spp, changing the random seed so it is not correlated with the input.

Animation and motion vectors. The animations in our training set are simple translations or rotations of the camera. We randomize the speed of the camera and render 8 consecutive frames per scene. We altered PBRT-v3 to generate per-sample motion vectors. We test whether the normal and world position in the current and previous frame agree after warping using the motion vectors, and discard motion vectors that fail this test.

4.2 Losses

We train our denoiser to reconstruct clean, temporally stable animations by minimizing a reconstruction loss, a temporal stability loss, and a regularization on the affinity parameters.

$$\mathcal{L} = \mathcal{L}_{\text{recons}} + 0.25 \cdot \mathcal{L}_{\text{temporal}} + 10^{-5} \cdot \mathcal{L}_{\text{reg}}. \tag{9}$$

We use the Symmetric Mean Absolute Percentage Error over the linear radiance (SMAPE) [Vogels et al. 2018] as our reconstruction loss:

$$\mathcal{L}_{\text{recons}} = \text{SMAPE}(\mathbf{O}, \mathbf{O}^\star), \tag{10}$$

where $\mathbf{O}^\star$ is the ground truth image. SMAPE is defined for two tensors A and B as:

$$\text{SMAPE}(A, B) = \frac{1}{3}\mathbb{E}_{xyt}\frac{\|A_{xyt} - B_{xyt}\|_1}{\|A_{xyt}\|_1 + \|B_{xyt}\|_1 + \epsilon}. \tag{11}$$

The expectation $\mathbb{E}$ is taken over pixels and frames, $\|.\|_1$ is the L_1 norm, and the factor 3 accounts for color channels.

To penalize inconsistency between successive frames, we use the temporal loss:

$$\mathcal{L}_{\text{temporal}} = \text{SMAPE}(\partial_t \mathbf{O}, \partial_t \mathbf{O}^\star), \tag{12}$$

with ∂_t the finite difference operator along the time dimension [Chaitanya et al. 2017].

Finally, our regularization is an L_2 penalty over the kernels' bandwidth parameters:

$$\mathcal{L}_{\text{reg}} = \sum_k \mathbb{E}_{xyt}\|a^k_{xyt}\|_2^2 + \mathbb{E}_{xyt}\|b_{xyt}\|_2^2. \tag{13}$$

We found that without this regularizer, the scale ambiguity between these parameters and the magnitude of the features $\mathbf{f}^k_{xyt}$ made the training numerically unstable.

4.3 Training details

Our denoiser is implemented in PyTorch [Paszke et al. 2019] and trained to convergence using the ADAM optimizer [Kingma and Ba 2014] with learning rate set to 10^{-4} and batch size 4; all other optimizer settings are kept at their default values. We augment our dataset with horizontal and vertical flips, 90 degrees rotation and random cropping of size 128×128. Training typically converges after 750 epochs, which takes roughly 5 days for our 8-frames animation dataset on a GeForce RTX 2080 Ti GPU and an Intel Xeon W-2235 CPU with 12 cores. Training a single-frame variant of our model (i.e., with no temporal filtering) takes about 2 days. We multiply the learning rate by 0.75 every 150 epochs. For the single-frame variant, we decrease the learning rate once to 5×10^{-5} when the validation loss plateaus, around epoch 600. During training, we select the number of samples $S \in \{1, 2, 4\}$ in a round-robin fashion at the beginning of each epoch (we use $S \in \{2, 4, 8\}$ for the single-image variant). We keep the model with the best validation loss at 4 spp (resp. 8 spp for the single-image task). We use 13×13 kernels during training but, because our kernels are computed from pairwise affinities, we can change the kernel size at test time.

5 RESULTS

We evaluate our denoiser on a test dataset of 26 publicly available scenes [Bitterli 2016; Pharr et al. 2016] converted and rendered with PBRT-v3 [Pharr et al. 2016]. We compare to state-of-the-art solutions for both interactive and off-line denoising on 26 static renderings and 6 videos . The videos are 120 frames long fly through animations,

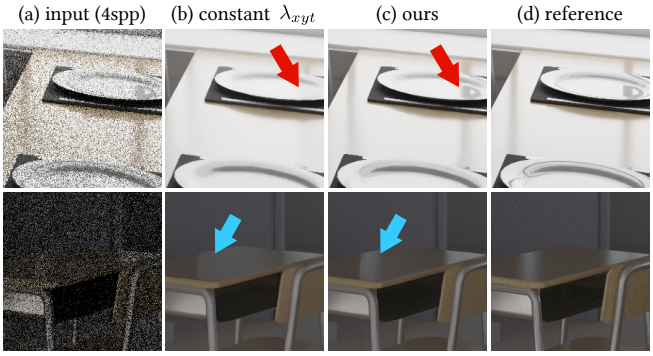

Fig. 6. **Benefit of learning** λ_{xyt}. Learning per-pixel blending weights in our temporal accumulation helps discard inconsistent reprojections in the warps, thus recovering better details in occluded areas and sharp specular reflections (c). We show an ablation of our model that fixes $\lambda_{xyt} = 0.8$ for all pixels, as is done in Koskela et al. [2019]; Meng et al. [2020]; Schied et al. [2017]. Without learnable blending weights, the model oversmoothes specular highlights (b).

rendered at 1920 × 1024 resolution. We render the ground truth images at 4096 spp, and the videos at 2048 spp. We use bidirectional path tracing [Lafortune and Willems 1993; Veach and Guibas 1995] for some scenes with complex light transport. The noisy inputs always use uni-directional path tracing.

Our algorithm outperforms previous work in both the single frame (§ 5.2) and animation setups (§ 5.3). It has better temporal stability and runs at interactive framerates (§ 5.4). We analyze the impact of our design choices in an ablation study (§ 5.5). Full resolution static and video results can be found in the supplemental material, together with additional quantitative metrics.

5.1 Baselines and metrics

We compare to three state-of-the-art off-line denoisers, KPCN [Bako et al. 2017], SBMC [Gharbi et al. 2019], and NDLE [Munkberg and Hasselgren 2020]; and two interactive methods, NBG [Meng et al. 2020] and OptiX (ONND), adapted from Chaitanya et al. [2017].

We implemented the two variants described by Munkberg and Hasselgren [2020]: *NDLE* is a high-quality but slower model; and *NDLE-ms* is an interactive, multi-scale variant. Unlike the original, our implementation of NDLE-ms is not optimized, so we exclude it from our speed comparison. We reimplemented NBG in PyTorch following the open-source implementation provided by the authors, and include a slower but higher-quality variant, NBG-large, which uses the U-Net architecture of our method in its *guide net*. We followed Bako et al. [2017] for our implementation of KPCN. We adapted the open-source code from Gharbi et al. [2019] for SBMC, adjusting the number of filters in the fully-connected and convolutional layers so that the total number of parameters roughly match NDLE (~ 18 million). We used the official OptiX 7.2 SDK[1] for ONND, which takes HDR radiance, normals and albedo as input, and produces HDR outputs. Unless otherwise specified we use the same input features for our method, NDLE, and SBMC. Since NDLE uses 17×17 kernels, we adopted the same kernel size for SBMC and KPCN, rather than their original 21 × 21 size. More details on the training and architecture of the baselines can be found in supplemental.

5.1.1 Evaluation metrics. For both single images and videos, we compare denoisers using the PSNR on the tonemapped radiance:

$$\mathrm{PSNR}(\mathbf{O}, \mathbf{O}^\star) = -10 \log_{10} \left(\frac{1}{3} \mathbb{E}_{xyt} \| \tau\, \mathbf{O}_{xyt} - \tau\, \mathbf{O}^\star_{xyt} \|_2^2 \right). \quad (14)$$

The expectation $\mathbb{E}$ is over pixels and frames, the factor 3 accounts for color channels, and τ is a tonemapping and gamma correction operator [Reinhard et al. 2002], defined pointwise as

$$\tau : x \in \mathbb{R}^+ \mapsto \left(\frac{x}{1+x} \right)^{\frac{1}{2.4}} \quad (15)$$

For animations, we also compute the Temporal Relative Mean Absolute Error (TRMAE), which we define as:

$$\mathrm{TRMAE}(\mathbf{O}, \mathbf{O}^\star) = \frac{1}{3} \mathbb{E}_{xyt} \frac{\| \partial_t \mathbf{O}_{xyt} - \partial_t \mathbf{O}^\star_{xyt} \|_1}{\| \partial_t \mathbf{O}^\star_{xyt} \|_1 + \epsilon}, \quad (16)$$

where $\epsilon = 0.01$ prevents the numerical instability. We find this metric to correlate well with perceptual evaluation as a temporal stability measure in our evaluations. We refer the reader to the supplemental material to see other metrics applied on the temporal gradients.

5.2 Single-frame comparison

We first evaluate our denoiser on static images, configuring all methods to process frames independently, one at a time. We disable our temporal accumulation (Eq. (3) and (5)) and temporal filtering (Eq. (8)) mechanisms, and call this single-frame variant *ours-single*. Our algorithm consistently outperforms recent interactive denoisers. It matches or outperforms off-line denoisers, for a fraction of the cost. Table 2 summarizes our evaluation, and Figure 14 shows a few examples. *Ours-K*1 uses a single 17 × 17 kernel like the kernel-predicting baselines. In Section 5.5.6, we discuss the advantage of using several, iteratively applied kernels instead of using a single large one. Full resolution images can be found in the supplemental.

5.3 Video denoising

Table 3 shows a quantitative comparison of our full model, with temporal filtering activated, against prior methods for video denoising. As in the single-frame experiment, our method achieves higher PSNR and lower TRMAE than prior methods. *Ours-wpred*, *ours-heur*, *ours-ntk* and *ours-nar* are ablations discussed in Section 5.5.4 and Section 5.5.5.

5.4 Implementation and performance

We optimized our model for inference, using cuDNN 8.0[2] to implement the fully-connected sample embedding network and the U-net, and exploiting half-precision floating-point operations for speed. We implemented other modules using custom CUDA kernels. Because cuDNN cannot fuse convolution-bias-activation operations unless the activation is ReLU, we replaced leaky ReLU with standard ReLU in our pretrained model then fine-tuned for 150 epochs We

[1] https://developer.nvidia.com/designworks/optix/download

[2] https://developer.nvidia.com/cudnn

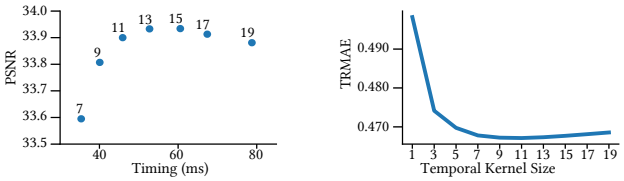

Fig. 7. **Quality of various kernel sizes vs. performance (optimized)** . On the left, we set the spatial and temporal kernel size to the same value from 7×7 to 19×19. We run our denoiser on a GeForce RTX 2080 Ti, and average the timings over 120 4spp frames of the *Bedroom* scene with resolution 1920×1024. On the right, we fix the spatial kernel size to 13×13, and vary the temporal kernel size from 1×1 to 19×19. PSNR (higher is better) and TRMAE (lower is better) values are averaged over 6 test videos.

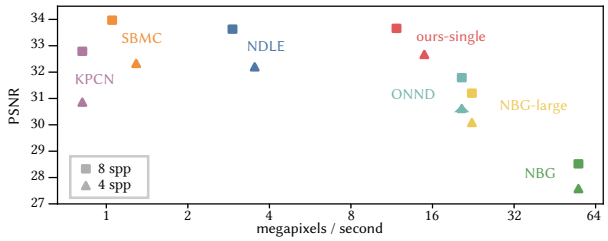

Fig. 8. **PSNR vs. throughput (unoptimized)**. With an unoptimized implementation, our method already achieves an appealing runtime/quality profile. Except ONND, for which we use the official release API, all the timings reported here use unoptimized PyTorch implementations. We report throughput in megapixels per second (log-scale). Top-right is better. PSNR results are averaged over 26 static test images. Table 1 shows a performance breakdown of our *optimized* implementation .

applied the same procedure to all models analyzed in Section 5.5.4 and Section 5.5.5. Table 1 shows the runtime cost of each component of the optimized implementation of our full, temporally-stable model. We analyze the effect of the kernel size on the final quality and performance of this optimized implementation in Figure 7, observing that 11×11 or 13×13 kernels give the best compromise.

For fair comparison with unoptimized baselines, we benchmarked our single-frame variant (*ours-single*) and the baselines directly in PyTorch. Figure 8 shows that even our unoptimized implementation offers near-interactive frame rates while achieving state-of-the-art results. It has only 0.94 million network parameters compared to the off-line baselines (SBMC: 18.04M, NDLE: 17.98M, KPCN: 5.08M).

5.5 Model ablations

In this section we examine: the effect of changing the kernel sizes at *test* time, how the affinity features' dimensionality impacts quality, alternative strategies for temporal stabilty, and the advantage of sample embeddings over mean/variance reduction of the input.

5.5.1 Dimension of the affinity features. The dimension of our affinity features directly affects the complexity of pairwise relationships our model can capture between pixels under the kernel. A low dimension d can only represent the simplest relationships (e.g., "identical color"). Table 4 summarizes our results. Using 1-dimensional

Table 1. **Performance breakdown.** Timings of our cuDNN implementation for 4spp inputs with 1920×1024 resolution using a GeForce RTX 2080 Ti graphics card. We use 13×13 spatial and temporal kernels.

Components	FC	U-Net	Kernels	Other	**Total**
Time (ms)	5.76	21.07	22.72	3.19	**52.74**

Table 2. **Quantitative evaluation on static single-frame denoising.** When processing a single image, our method is competitive with state-of-the-art off-line denoisers that have a significantly higher computational cost (first group), and it consistently outperforms interactive denoisers (second group). Starred method (*) were designed to account for temporal stability. We highlight the first and second best result in each column. Higher PSNR (resp. lower SMAPE) is better.

	PSNR				
method	2spp	4spp	8spp	16spp	32spp
KPCN	27.95	30.86	32.79	33.90	34.54
SBMC	28.97	32.33	33.97	34.57	34.44
NDLE	30.08	32.20	33.63	34.45	34.73
NDLE-ms	29.47	31.81	33.14	33.87	34.12
ONND	29.40	30.62	31.79	32.88	33.91
NBG*	26.04	27.58	28.52	29.11	29.42
NBG-large*	28.58	30.09	31.20	31.94	32.58
ours-$K1$	29.13	31.87	33.28	34.11	34.42
ours-single	30.93	32.67	33.66	34.34	34.81

Table 3. **Quantitative evaluation on video denoising.** The first three groups are: single-frame off-line denoisers, interactive denoisers, and ablations (§ 5.2, § 5.5.4 and § 5.5.5) on our technique. Starred method (*) were not designed to handle videos, in particular they make no attempt at temporal stability, hence the relatively higher TRMAE values. We highlight the first and second best result in each column. Higher PSNR (resp. lower TRMAE) is better.

	PSNR			TRMAE		
method	2spp	4spp	8spp	2spp	4 spp	8spp
NDLE*	30.98	33.05	34.37	0.764	0.618	0.571
NDLE-ms*	31.02	32.91	33.96	0.806	0.662	0.595
ONND*	30.66	31.74	32.74	1.988	1.693	1.468
NBG	26.67	28.48	29.56	2.058	1.695	1.453
NBG-large	29.31	30.67	31.60	1.069	1.001	0.906
ours-$K1$*	30.48	32.64	33.97	0.803	0.650	0.565
ours-single*	32.17	33.67	34.54	0.640	0.556	0.511
ours-wpred	32.18	33.48	34.33	0.513	0.482	0.462
ours-heur	32.05	32.89	33.33	0.511	0.485	0.472
ours-ntk	32.55	33.79	34.44	0.502	0.474	0.457
ours-nar	32.37	33.76	34.56	0.508	0.473	0.454
ours	32.34	33.93	34.81	0.517	0.467	0.446

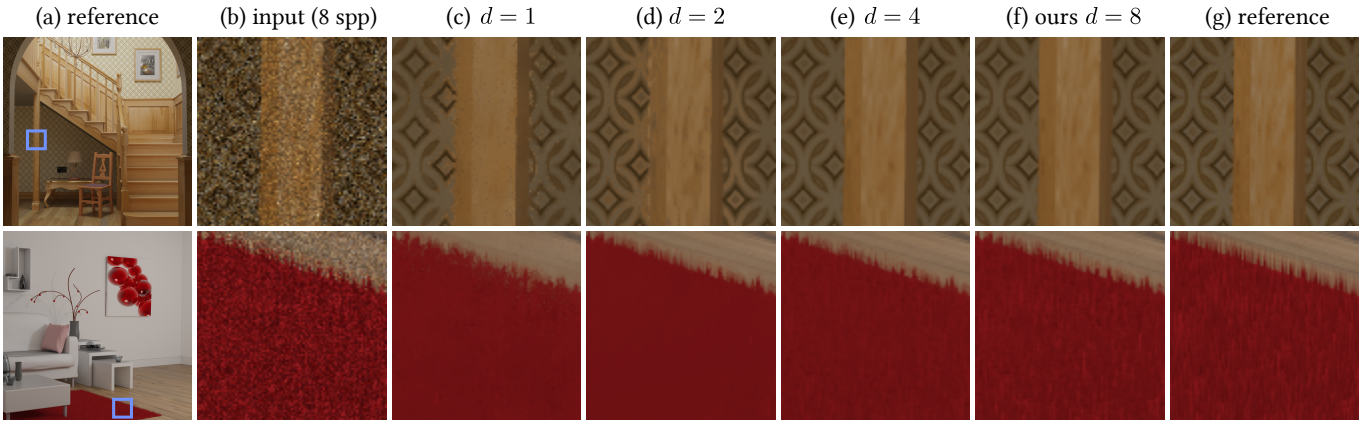

Fig. 9. **Impact of the affinity feature dimension d on quality**. On the top row, we show how dimensionality affects the reconstruction of the fine details in the albedo. Using fewer features in the learned affinity, our denoiser with $d = 1$ cannot reconstruct the texture of the wooden wall and leaves high-frequency artifacts (c). When $d = 2$, our method cannot effectively distinguish the wooden block from the wall behind it, the color of the wooden block smears onto the wall (d). As we increase the dimension of the affinity features to $d = 4$ (e) and $d = 8$ (f), our reconstruction of high-frequency albedo improves significantly. The bottom row shows a similar behavior for high frequency geometric details. Using $d = 1$ leaves jaggy artifacts (c) whereas with $d = 2$, most of the details on the red carpet are blurred (d). As the dimension increases to $d = 4$ (e) and $d = 8$ (f) our model reconstructs most of the details. For these examples, we did not observe further improvements for d larger than 8.

features leads to significantly worse results, which can explain the limited performance of NBG (see Section 3.7, Table 2 and Table 3). Quantitatively, we do not observe significant variations for $d \geq 2$ (Table 4), but Figure 9 shows the difference can be striking. With too small a dimension, the denoised results lose high-frequency details.

5.5.2 No sample embeddings. To analyze the impact of our sample embeddings (§ 3.2), we compare to two ablations. Detailed results are provided in supplemental. The first ablation (*ours-me*) averages the raw feature buffers *before* the sample embedding network (FC in Eq. (1)), unlike our method which averages *after* FC. This ablation performs favorably at 2 spp, but does not generalize well to higher sample counts. The second ablation (*ours-pixel*) disables FC altogether and directly computes the mean and variance of the raw input buffers instead. It performs well at higher sample counts (16–32 spp), but does not generalize to lower sample counts, where variance estimation is less reliable. Most importantly, although it performs on par with our method numerically (e.g., at 8 spp), it exhibits high-frequency artifacts when the input feature buffers are severely undersampled (Figure 10). Our method generalizes well to all sample counts. Its advantages are most salient at the low sample counts typical for interactive rendering.

5.5.3 Changing the kernel size at runtime. We use 13×13 kernels during training, but because we predict feature vectors instead of kernels directly, we can arbitrarily change the kernel size at test time. Table 5 shows the impact of varying kernel sizes, for several sample counts. It suggests smaller kernels are sufficient at higher sample counts (less noise). Even though changing the kernel size leads only to minor quantitative differences, Figure 11 demonstrates that using a sufficiently small kernel size causes low-frequency noise artifacts. The noise can be reduced by using a larger spatial context. This can be achieved either by enlarging the spatial kernels or by

Table 4. **Ablation on the affinity features dimension d.** Increasing the dimension of the affinity features $\mathbf{f}^k_{xyt}$ gives more discriminative power to our kernels, improving quality. This evaluation is done using ours-single model on static images. See Figure 9 for qualitative differences.

	PSNR				
feature size	2spp	4spp	8spp	16spp	32spp
$d = 1$	26.65	27.77	28.25	28.44	28.55
$d = 2$	30.23	31.98	32.97	33.61	34.04
$d = 4$	30.73	32.43	33.40	34.06	34.53
$d = 8$ (ours)	30.93	**32.68**	33.67	34.34	34.81
$d = 12$	**30.97**	32.62	33.64	34.35	**34.86**
$d = 16$	30.11	32.63	**33.76**	**34.44**	34.81

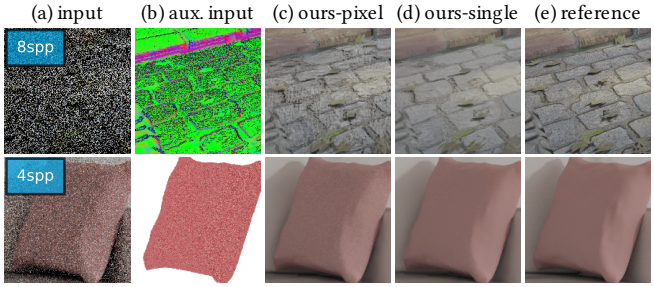

Fig. 10. **Samples embeddings vs. summary statistics.** Mapping the raw sample feature buffers (b, one map shown) to learned embeddings prior to averaging outperforms simple statistics, especially when using few samples. The simple simple statistics ablation leaves high-frequency artifacts (c) when the auxiliary buffers are noisy due to undersampled geometry (b, top) or undersampled albedo (b, bottom). Our method (d) with sample encoding distinguishes the noise from the data, producing clean results.

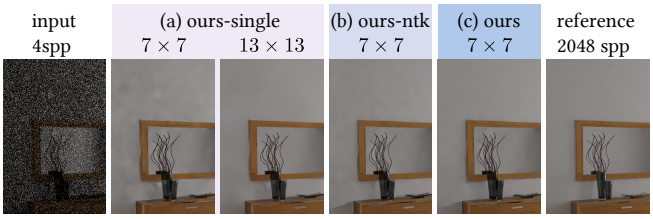

Fig. 11. **Visual impact of the kernel size and temporal denoising**. In highly noisy scenes, a single-frame denoiser can leave perceptually salient low-frequency residual noise (a, 7×7). Using larger kernels (a, 13×13) mitigates this issue. The ablation with no temporal kernels (b) exhibits low-frequency artifacts for smaller kernels, but still significantly improves upon our single-frame variant (a) because it benefits from our temporal accumulation scheme. Our full model further improves denoising quality thanks to temporal kernels, which expand the filtering footprint in time (c).

means of temporal filtering mechanisms, which effectively lets the method use a larger spatial footprint.

5.5.4 Temporal accumulation. We show the importance of temporally accumulating features (Eq. (3)) and radiance (Eq. (5)), by disabling both mechanisms, but keeping the temporal kernel. In this ablation, *ours-wpred*, we replace the warped previous sample embeddings in the U-net's inputs ($\mathcal{W}_t \bar{\mathbf{e}}_{xy,t-1}$ in Eq. (2)) with the warped previous *prediction*. This strategy is inspired by Hasselgren et al. [2020]. In a second ablation, *ours-heur*, we replace our learned per-pixel temporal blending weight with a constant $\lambda_{xyt} = 0.8$ [Koskela et al. 2019; Meng et al. 2020; Schied et al. 2017]. This ablation cannot properly reconstruct view-dependent effects (Fig. 6). Table 3 shows both ablations reduce quality (up to $\sim$ 1.5dB PSNR), suggesting that our temporal accumulation scheme with adaptive weights is key.

5.5.5 Temporal filtering. In *ours-ntk*, we disable the temporal kernel (§ 3.5.2) but keep the temporal accumulation mechanism. Unlike our full model, this ablation cannot completely remove low-frequency noise (Fig. 11). Table 3 shows the temporal kernel of our full method is more beneficial at larger sampler counts (> 2spp), i.e., the model benefits less from the previous denoised frame when noise is severe.

Using both a temporal kernel and temporal radiance accumulation (Eq. (5)) might seem redundant. In *ours-nar*, we disable radiance accumulation to show this is not the case. The pixel embeddings are still accumulated temporally, so the U-Net can still produce reliable features, benefiting from an effectively higher sample count. Radiance accumulation is more effective at higher sample counts (Table 3).

5.5.6 Affinity-based kernels vs. gather kernels. To better understand their properties, we run an ablation where our affinity-based kernels are replaced with full-rank gather kernels [Bako et al. 2017] (labeled *gather*). Furthermore, we run this comparison for $K = 1$ and $K = 3$ kernels to illustrate the advantages of our sequential dilated filtering approach. Except for the last convolution, whose channel count depends on the kernel size, the ablation's architecture is identical to our full model. This analysis is summarized in Table 5.

In the single kernel case ($K = 1$ with no dilation in Section 3.3), gather kernels numerically outperform our affinities. However, both

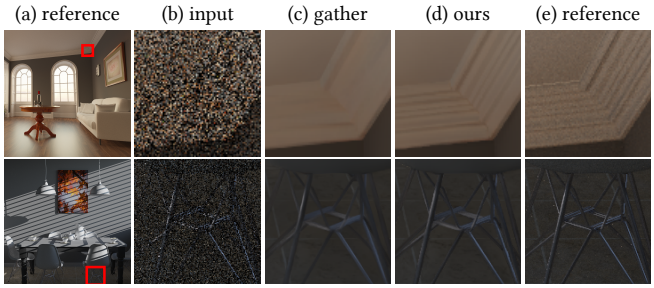

Fig. 12. **Affinity-based kernels recover fine details better.** By looking at the Table 5 to decide the optimal kernel sizes, we choose 9×9 with $K = 3$ for gather. For fair runtime usage, we choose 9×9 with $K = 3$ for our method despite obtaining better results for larger kernel sizes. Affinity-based kernels (d) are better at reconstructing fine geometric details (top) as well as high-frequency reflections (bottom) both of which are blurred by gather kernels (c).

approaches create block artifacts (images in supplemental) because the kernels are too small to be effective, suggesting a larger spatial context is needed. Iteratively filtering with $K = 3$ dilated kernels, yields a much larger spatial support, from which our affinity-based kernels benefit significantly, outpeforming gather kernels. The improvements are much more modest for gather kernels.

The advantage of our affinities becomes clearer with large kernels, where modeling complex pairwise interactions between pixels is challenging. Overall, affinity-based kernels are significantly better at reconstructing high-frequency details (Figure 12). Conversely, visual inspection shows that gather kernels are better at removing low-frequency noise at low sample counts, when the kernel size is small (the top-left region of the Table 5 is dominated by gather). Still, together with our multi-scale dilation and temporal filtering strategies, our affinity-based kernels can filter low-frequency noise better.

Finally, the memory access pattern of gather kernels make them more efficient to apply to the noisy image. However, they require a final convolution layer with significantly more parameters (quadratic in the kernel size) than our affinities (constant size), so that, overall, both approaches have roughly the same execution time. Gather kernels require more memory as the kernel size increases. This tilts the runtime balance in favor of our affinity-based kernels. The supplemental material shows a numerical comparison on memory and runtime performance, and additional visual comparisons.

5.6 Limitations

We visualize some of the limitations of our denoiser in Figure 13. First, our training dataset does not contain renderings with distributed effects, such as motion blur and depth of field which limits the capability of our method to generalize to such scenes. Second, we have difficulty with light transport scenarios where highly contributing paths are sampled with very low probabilities during the rendering process. In future work, it is natural to explore connecting the denoiser with a neural importance sampling network [Müller et al. 2019]. Third, we generate motion vectors only at the first intersection point for each pixel during the rendering process, which

Table 5. **Quantitative comparison between the affinity-based kernels (ours) and gather kernels.** The PSNR results of each method on the static-image test scenes are shown. For each spp and kernel size pair, we use different colors to highlight whether affinity-based or gather is the best. The best PSNR result for each spp is highlighted in **bold**. Number of kernel entries is the representative of the respective kernel's runtime and storage (only for gather) cost.

		$K=1$								$K=3$				
		9×9	11×11	13×13	15×15	17×17	19×19	21×21	23×23	5×5	7×7	9×9	11×11	13×13
2spp	ours	27.58	28.19	28.61	28.91	29.13	29.28	29.38	29.44	29.43	30.19	30.57	30.79	30.93
	gather	30.11	29.13	30.43	30.25	29.18	30.40	29.02	30.26	30.23	30.61	**30.98**	30.69	30.82
4spp	ours	30.39	31.00	31.40	31.67	31.87	32.00	32.07	32.10	31.68	32.26	32.50	32.62	**32.67**
	gather	32.03	31.94	32.29	32.31	31.98	32.39	32.11	32.37	32.29	32.35	32.51	32.44	32.50
8spp	ours	32.15	32.63	32.94	33.14	33.28	33.36	33.40	33.41	33.10	33.49	33.63	**33.67**	33.66
	gather	33.14	33.31	33.34	33.42	33.30	33.43	33.50	33.38	33.35	33.36	33.41	33.34	33.44
16spp	ours	33.31	33.67	33.88	34.02	34.11	34.14	34.15	34.14	34.10	34.33	**34.39**	34.38	34.34
	gather	33.93	34.20	34.10	34.16	34.10	34.15	34.36	34.08	34.13	34.07	34.02	33.77	34.11
32spp	ours	33.95	34.18	34.31	34.38	34.42	34.43	34.41	34.38	34.85	34.95	34.93	34.88	34.81
	gather	34.53	34.80	34.67	34.65	34.60	34.72	**34.97**	34.60	34.64	34.58	34.45	33.17	34.53
kernel entries		81	121	169	225	289	361	441	529	75	147	243	363	507

cannot model the true warping of the specular regions. So, for highly specular materials, we do not generate motion vectors. See the "bedroom" and "bathroom" scenes in the supplemental video for such examples that cause temporal artifacts.

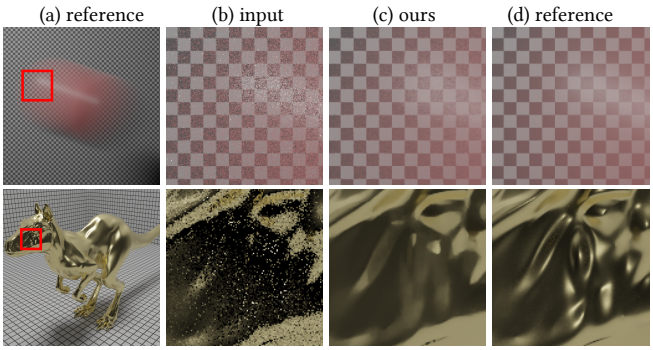

Fig. 13. **Limitations**. The top row (a) shows a motion blurred sphere in front a of a static checkberboard. Our method (c) was not trained to handle motion blur, so it fails to spread the samples sufficiently to reconstruct the smooth gradient shown in the reference (d). The bottom row shows a specular material. A 2 spp input (b) is too severely under-sampled to properly reconstruct the metallic reflection.

6 CONCLUSION

We have presented a novel method for denoising Monte Carlo renderings at interactive speeds with quality on-par with off-line denoisers. We use an efficient network to aggregate relevant per-sample features into temporally-stable per-pixel features. Pairwise affinity between these features are used to predict dilated 2D kernels that are iteratively applied to the input radiance to produce the final denoised result. We show our model can spatially adjust the kernels to effectively smooth out noise and preserve fine details. We further demonstrate how to incorporate the spatially-warped content from previous frames to produce a temporally consistent result.

ACKNOWLEDGMENTS

We thank Sebastian Weiß for his valuable feedback, Jacob Munkberg and Josef Stumpfegger for their help with the previous work, and the anonymous Siggraph reviewers for their precious suggestions.

REFERENCES

Steve Bako, Thijs Vogels, Brian McWilliams, Mark Meyer, Jan Novák, Alex Harvill, Pradeep Sen, Tony Derose, and Fabrice Rousselle. 2017. Kernel-predicting convolutional networks for denoising Monte Carlo renderings. *ACM Trans. Graph.* 36, 4 (2017), 97–1.

Pablo Bauszat, Martin Eisemann, S John, and M Magnor. 2015. Sample-based manifold filtering for interactive global illumination and depth of field. *Computer Graphics Forum* (2015).

Pablo Bauszat, Martin Eisemann, and Marcus Magnor. 2011. Guided Image Filtering for Interactive High-quality Global Illumination. *Computer Graphics Forum (Proc. EGSR)* (2011).

Laurent Belcour, Cyril Soler, Kartic Subr, Nicolas Holzschuch, and Fredo Durand. 2013. 5D covariance tracing for efficient defocus and motion blur. *ACM TOG* (2013).

Benedikt Bitterli. 2016. Rendering resources. https://benedikt-bitterli.me/resources.

Benedikt Bitterli, Fabrice Rousselle, Bochang Moon, José A. Iglesias-Guitián, David Adler, Kenny Mitchell, Wojciech Jarosz, and Jan Novák. 2016. Nonlinearly Weighted First-order Regression for Denoising Monte Carlo Renderings. *Computer Graphics Forum (Proc. EGSR)* (2016).

Chakravarty R Alla Chaitanya, Anton S Kaplanyan, Christoph Schied, Marco Salvi, Aaron Lefohn, Derek Nowrouzezahrai, and Timo Aila. 2017. Interactive reconstruction of Monte Carlo image sequences using a recurrent denoising autoencoder. *ACM Transactions on Graphics (TOG)* 36, 4 (2017), 1–12.

Angel X. Chang, Thomas Funkhouser, Leonidas Guibas, Pat Hanrahan, Qixing Huang, Zimo Li, Silvio Savarese, Manolis Savva, Shuran Song, Hao Su, Jianxiong Xiao, Li Yi, and Fisher Yu. 2015. *ShapeNet: An Information-Rich 3D Model Repository.* Technical Report arXiv:1512.03012 [cs.GR]. Stanford University — Princeton University — Toyota Technological Institute at Chicago.

M. Cimpoi, S. Maji, I. Kokkinos, S. Mohamed, , and A. Vedaldi. 2014. Describing Textures in the Wild. In *Proceedings of the IEEE Conf. on Computer Vision and Pattern Recognition (CVPR).*

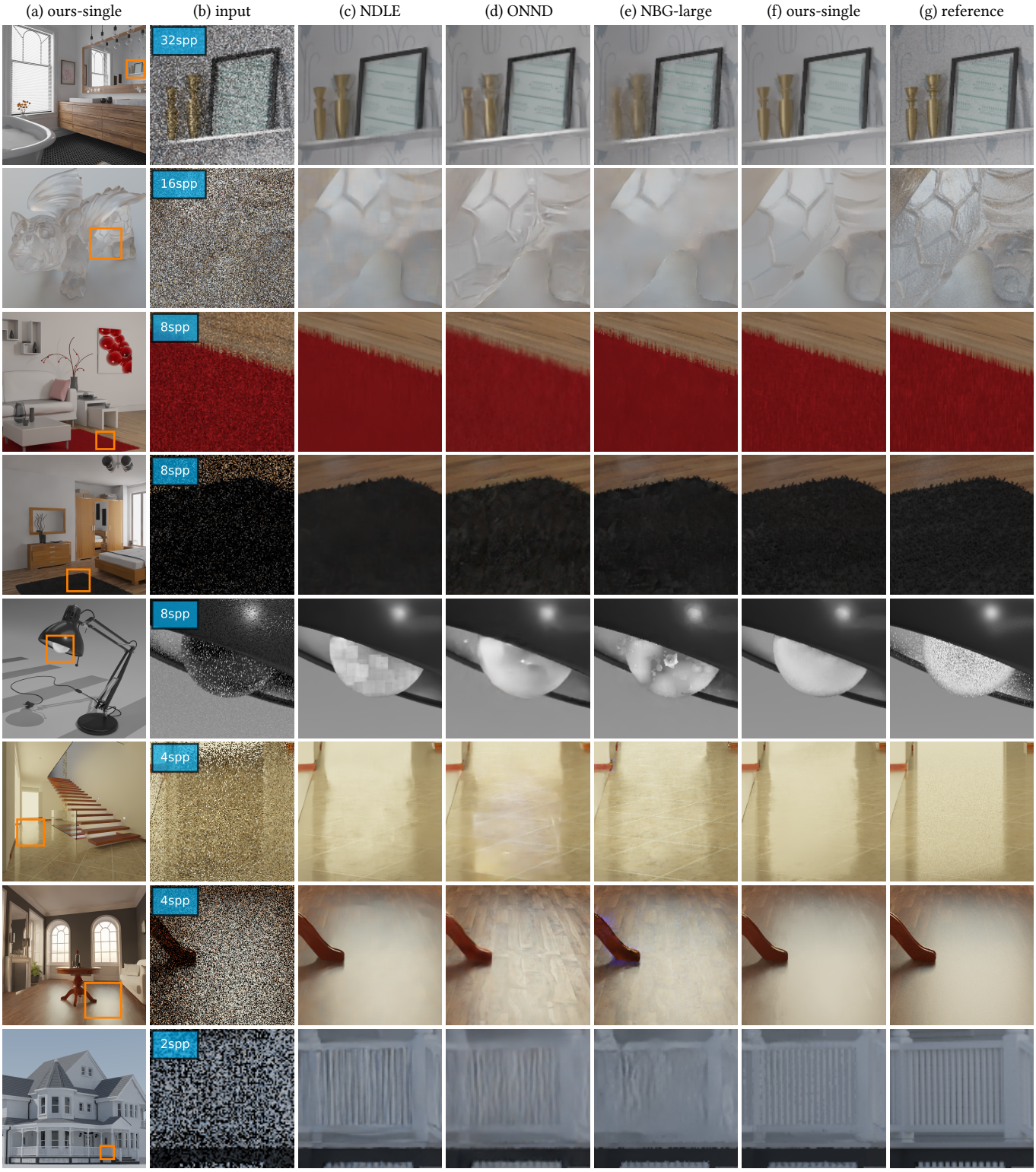

Fig. 14. **Qualitative comparison on single-frame denoising.** Our method (a) and (f) produces noticeably cleaner outputs than previous interactive techniques (d,e), especially around specular materials. It often resolves fine details better than state-of-the-art offline methods (c).

Holger Dammertz, Daniel Sewtz, Johannes Hanika, and Hendrik PA Lensch. 2010. Edge-avoiding À-Trous wavelet transform for fast global illumination filtering. In *Proceedings of the Conference on High Performance Graphics*. Citeseer, 67–75.

Mauricio Delbracio, Pablo Musé, Antoni Buades, Julien Chauvier, Nicholas Phelps, and Jean-Michel Morel. 2014. Boosting monte carlo rendering by ray histogram fusion. *ACM Transactions on Graphics (TOG)* 33, 1 (2014), 1–15.

Frédo Durand, Nicolas Holzschuch, Cyril Soler, Eric Chan, and François X Sillion. 2005. A frequency analysis of light transport. *ACM SIGGRAPH* (2005).

Kevin Egan, Florian Hecht, Frédo Durand, and Ravi Ramamoorthi. 2011. Frequency analysis and sheared filtering for shadow light fields of complex occluders. *ACM TOG* (2011).

Kevin Egan, Yu-Ting Tseng, Nicolas Holzschuch, Frédo Durand, and Ravi Ramamoorthi. 2009. Frequency analysis and sheared reconstruction for rendering motion blur. *ACM SIGGRAPH* (2009).

Michaël Gharbi, Jiawen Chen, Jonathan T Barron, Samuel W Hasinoff, and Frédo Durand. 2017. Deep bilateral learning for real-time image enhancement. *ACM Transactions on Graphics (TOG)* 36, 4 (2017), 1–12.

Michaël Gharbi, Tzu-Mao Li, Miika Aittala, Jaakko Lehtinen, and Frédo Durand. 2019. Sample-based Monte Carlo denoising using a kernel-splatting network. *ACM Transactions on Graphics (TOG)* 38, 4 (2019), 1–12.

Toshiya Hachisuka, Wojciech Jarosz, Richard Peter Weistroffer, Kevin Dale, Greg Humphreys, Matthias Zwicker, and Henrik Wann Jensen. 2008. Multidimensional adaptive sampling and reconstruction for ray tracing. *ACM SIGGRAPH* (2008).

J. Hasselgren, J. Munkberg, M. Salvi, A. Patney, and A. Lefohn. 2020. Neural Temporal Adaptive Sampling and Denoising. *Computer Graphics Forum* 39 (2020).

Kaiming He, Jian Sun, and Xiaoou Tang. 2010. Guided image filtering. *ECCV* (2010).

Matthias Holschneider, Richard Kronland-Martinet, Jean Morlet, and Ph Tchamitchian. 1990. A real-time algorithm for signal analysis with the help of the wavelet transform. In *Wavelets*. Springer, 286–297.

James T. Kajiya. 1986. The Rendering Equation. *ACM SIGGRAPH* (1986).

Nima Khademi Kalantari, Steve Bako, and Pradeep Sen. 2015. A machine learning approach for filtering Monte Carlo noise. *ACM Trans. Graph.* 34, 4 (2015), 122–1.

Nima Khademi Kalantari and Pradeep Sen. 2013. Removing the noise in Monte Carlo rendering with general image denoising algorithms. *Computer Graphics Forum (Proc. EG)* (2013).

Markus Kettunen, Erik Härkönen, and Jaakko Lehtinen. 2019. Deep convolutional reconstruction for gradient-domain rendering. *ACM Transactions on Graphics (TOG)* 38, 4 (2019), 1–12.

Khronos. 2020. *Vulkan 1.2.167 Specification.* https://www.khronos.org/registry/vulkan/specs/1.2-extensions/html/vkspec.html

Diederik P Kingma and Jimmy Ba. 2014. Adam: A method for stochastic optimization. *arXiv preprint arXiv:1412.6980* (2014).

Matias Koskela, Kalle Immonen, Markku Mäkitalo, Alessandro Foi, Timo Viitanen, Pekka Jääskeläinen, Heikki Kultala, and Jarmo Takala. 2019. Blockwise multi-order feature regression for real-time path-tracing reconstruction. *ACM Transactions on Graphics (TOG)* 38, 5 (2019), 1–14.

Alexandr Kuznetsov, Nima Khademi Kalantari, and Ravi Ramamoorthi. 2018. Deep Adaptive Sampling for Low Sample Count Rendering. In *Computer Graphics Forum*, Vol. 37. Wiley Online Library, 35–44.

Eric P Lafortune and Yves D Willems. 1993. Bi-directional path tracing. (1993).

Jaakko Lehtinen, Timo Aila, Jiawen Chen, Samuli Laine, and Frédo Durand. 2011. Temporal light field reconstruction for rendering distribution effects. *ACM SIGGRAPH* (2011).

Jaakko Lehtinen, Timo Aila, Samuli Laine, and Frédo Durand. 2012. Reconstructing the indirect light field for global illumination. *ACM SIGGRAPH* (2012).

Tzu-Mao Li, Yu-Ting Wu, and Yung-Yu Chuang. 2012. SURE-based optimization for adaptive sampling and reconstruction. *ACM SIGGRAPH Asia* (2012).

Michael Mara, Morgan McGuire, Benedikt Bitterli, and Wojciech Jarosz. 2017. An efficient denoising algorithm for global illumination. *High Performance Graphics* 10 (2017), 3105762–3105774.

Xiaoxu Meng, Quan Zheng, Amitabh Varshney, Gurprit Singh, and Matthias Zwicker. 2020. Real-time Monte Carlo Denoising with the Neural Bilateral Grid. In *Eurographics Symposium on Rendering - DL-only Track*, Carsten Dachsbacher and Matt Pharr (Eds.). The Eurographics Association. https://doi.org/10.2312/sr.20201133

Microsoft. 2021. *DirectX Raytracing (DXR) Functional Spec.* https://microsoft.github.io/DirectX-Specs/d3d/Raytracing.html

Bochang Moon, Nathan Carr, and Sung-Eui Yoon. 2014. Adaptive rendering based on weighted local regression. *ACM TOG* (2014).

Bochang Moon, Steven McDonagh, Kenny Mitchell, and Markus Gross. 2016. Adaptive polynomial rendering. *ACM Transactions on Graphics (TOG)* 35, 4 (2016), 1–10.

Thomas Müller, Brian McWilliams, Fabrice Rousselle, Markus Gross, and Jan Novák. 2019. Neural importance sampling. *ACM Transactions on Graphics (TOG)* 38, 5 (2019), 1–19.

Jacob Munkberg and Jon Hasselgren. 2020. Neural Denoising with Layer Embeddings. In *Computer Graphics Forum*, Vol. 39. Wiley Online Library, 1–12.

Ryan S Overbeck, Craig Donner, and Ravi Ramamoorthi. 2009. Adaptive wavelet rendering. *ACM SIGGRAPH Asia* (2009).

Steven G. Parker, Heiko Friedrich, David Luebke, Keith Morley, James Bigler, Jared Hoberock, David McAllister, Austin Robison, Andreas Dietrich, Greg Humphreys, Morgan McGuire, and Martin Stich. 2013. GPU Ray Tracing. *Commun. ACM* 56, 5 (May 2013), 93–101. https://doi.org/10.1145/2447976.2447997

Adam Paszke, Sam Gross, Francisco Massa, Adam Lerer, James Bradbury, Gregory Chanan, Trevor Killeen, Zeming Lin, Natalia Gimelshein, Luca Antiga, Alban Desmaison, Andreas Kopf, Edward Yang, Zachary DeVito, Martin Raison, Alykhan Tejani, Sasank Chilamkurthy, Benoit Steiner, Lu Fang, Junjie Bai, and Soumith Chintala. 2019. PyTorch: An Imperative Style, High-Performance Deep Learning Library. In *Advances in Neural Information Processing Systems 32*, H. Wallach, H. Larochelle, A. Beygelzimer, F. d'Alché-Buc, E. Fox, and R. Garnett (Eds.). Curran Associates, Inc., 8024–8035. http://papers.neurips.cc/paper/9015-pytorch-an-imperative-style-high-performance-deep-learning-library.pdf

Matt Pharr, Wenzel Jakob, and Greg Humphreys. 2016. *Physically based rendering: From theory to implementation.* Morgan Kaufmann.

Erik Reinhard, Michael Stark, Peter Shirley, and James Ferwerda. 2002. Photographic tone reproduction for digital images. In *Proceedings of the 29th annual conference on Computer graphics and interactive techniques*. 267–276.

Olaf Ronneberger, Philipp Fischer, and Thomas Brox. 2015. U-net: Convolutional networks for biomedical image segmentation. In *International Conference on Medical image computing and computer-assisted intervention*. Springer, 234–241.

Fabrice Rousselle, Claude Knaus, and Matthias Zwicker. 2011. Adaptive Sampling and Reconstruction Using Greedy Error Minimization. *ACM Trans. Graph.* 30, 6 (Dec. 2011), 1–12. https://doi.org/10.1145/2070781.2024193

Fabrice Rousselle, Claude Knaus, and Matthias Zwicker. 2012. Adaptive rendering with non-local means filtering. *ACM SIGGRAPH Asia* (2012).

Fabrice Rousselle, Marco Manzi, and Matthias Zwicker. 2013. Robust denoising using feature and color information. In *Computer Graphics Forum*, Vol. 32. Wiley Online Library, 121–130.

Christoph Schied, Anton Kaplanyan, Chris Wyman, Anjul Patney, Chakravarty R. Alla Chaitanya, John Burgess, Shiqiu Liu, Carsten Dachsbacher, Aaron Lefohn, and Marco Salvi. 2017. Spatiotemporal Variance-guided Filtering: Real-time Reconstruction for Path-traced Global Illumination. *High Performance Graphics* (2017).

Christoph Schied, Christoph Peters, and Carsten Dachsbacher. 2018. Gradient estimation for real-time adaptive temporal filtering. *Proceedings of the ACM on Computer Graphics and Interactive Techniques* 1, 2 (2018), 1–16.

Pradeep Sen and Soheil Darabi. 2012. On filtering the noise from the random parameters in Monte Carlo rendering. *ACM TOG* (2012).

Carlo Tomasi and Roberto Manduchi. 1998. Bilateral filtering for gray and color images. In *Sixth international conference on computer vision (IEEE Cat. No. 98CH36271)*. IEEE, 839–846.

Eric Veach and Leonidas Guibas. 1995. Bidirectional estimators for light transport. In *Photorealistic Rendering Techniques*. Springer, 145–167.

Thijs Vogels, Fabrice Rousselle, Brian McWilliams, Gerhard Röthlin, Alex Harvill, David Adler, Mark Meyer, and Jan Novák. 2018. Denoising with kernel prediction and asymmetric loss functions. *ACM Transactions on Graphics (TOG)* 37, 4 (2018), 1–15.

Yue Wu, Brian Tracey, Premkumar Natarajan, and Joseph P Noonan. 2013. James–Stein type center pixel weights for non-local means image denoising. *IEEE Signal Processing Letters* 20, 4 (2013), 411–414.

Bing Xu, Junfei Zhang, Rui Wang, Kun Xu, Yong-Liang Yang, Chuan Li, and Rui Tang. 2019. Adversarial Monte Carlo denoising with conditioned auxiliary feature modulation. *ACM Trans. Graph.* 38, 6 (2019), 224–1.

Fisher Yu and Vladlen Koltun. 2016. Multi-Scale Context Aggregation by Dilated Convolutions. In *ICLR*.

M. Zwicker, W. Jarosz, J. Lehtinen, B. Moon, R. Ramamoorthi, F. Rousselle, P. Sen, C. Soler, and S.-E. Yoon. 2015. Recent Advances in Adaptive Sampling and Reconstruction for Monte Carlo Rendering. *Computer Graphics Forum (Proc. EG)* (2015).